Declining runoff sensitivity to precipitation following permafrost degradation: Insights from event-scale runoff response in the Yellow River source region

Zhuoyi Tu[1], Taihua Wang[2,3], Juntai Han[2,3], Hansjörg Seybold[4], Shaozhen Liu[4], Cansu Culha[4,5], Yuting Yang[2,3*], James W. Kirchner[4,6*]

5 [1]Jiangsu Key Laboratory of Soil and Water Processes in Watershed, College of Geography and Remote Sensing, Hohai University, Nanjing, 211100, China.

[2]State Key Laboratory of Hydroscience and Engineering, Tsinghua University, Beijing, 100084, China.

[3]Department of Hydraulic Engineering, Tsinghua University, Beijing, 100084, China.

[4]Department of Environmental System Sciences, ETH Zurich, Zurich, CH-8092, Switzerland

10 [5]Department of Earth, Ocean and Atmospheric Sciences, University of British Columbia, Vancouver, V6T 1Z4, Canada

[6]Swiss Federal Research Institute WSL, Birmensdorf, CH-8903, Switzerland

Correspondence to: Yuting Yang (yuting_yang@tsinghua.edu.cn), James Kirchner (kirchner@env.ethz.ch)

Abstract. Frozen ground, including permafrost and seasonally frozen ground (SFG), is a critical component of the cryosphere. Rapid atmospheric warming has accelerated the degradation of frozen ground, profoundly altering hydrological 15 processes in cold regions and affecting downstream water resources. Here we investigate the impacts of frozen ground degradation on event-scale runoff responses to daily precipitation in the source region of the Yellow River (SRYR) on the northeastern Tibetan Plateau using ensemble rainfall-runoff analysis (ERRA). ERRA is a data-driven, nonparametric, and model-independent method that quantifies dynamic, nonlinear, and spatially heterogeneous linkages between streamflow and precipitation. Applying ERRA, we evaluate changes in daily precipitation-streamflow coupling within the permafrost region, 20 where frozen soil depth has decreased by ~0.1 m per decade, and within the SFG region, where frozen soil depth has remained relatively stable, declining by only 0.03 m per decade. Between 1979–1998 and 1999–2018, the permafrost zone experienced a 47% reduction in peak runoff response per unit precipitation and a 32% decrease in the 25-day runoff coefficient. By contrast, no substantial changes in runoff response were observed in the SFG region. Rising temperatures and increased active layer thickness in the permafrost zone have substantially reduced streamflow sensitivity to precipitation, 25 particularly under higher precipitation intensities. Specifically, for daily precipitation intensities exceeding 10 mm d^{-1}, peak runoff response in the permafrost zone declined by 73% and the 25-day runoff coefficient declined by 72% between the two periods. These changes likely result from increased hydraulic connectivity and water storage capacity within the thawing active layer, facilitating increased infiltration and subsurface storage. Our findings underscore the effectiveness of data-driven methods in capturing hydrological regime shifts and offer critical insights for drought mitigation and flood risk 30 assessment in permafrost-affected regions amid ongoing climate warming.

1 Introduction

Frozen ground, including permafrost and seasonally frozen ground (SFG), is a key component of the cryosphere, covering approximately 50% of the land surface in the Northern Hemisphere (Qin et al., 2021; Zhang et al., 1999). As these frozen ground areas predominantly occur in high-latitude and high-altitude regions experiencing accelerated warming rates relative to the global average (Cohen et al., 2014; Pepin et al., 2015), they serve as sensitive indicators of climate change. With ongoing climate warming, significant degradation of frozen ground has been observed, including marked increases in ground temperature, active layer thickness of permafrost (Biskarborn et al., 2019; Luo et al., 2016), and persistent decreases in the maximum frozen depth of SFG (Frauenfeld and Zhang, 2011; Yang et al., 2023). These changes are having widespread impacts on hydrological, ecological, and environmental processes (Hjort et al., 2022; Mu et al., 2020; Schuur et al., 2015; Walvoord and Kurylyk, 2016; Wang et al., 2020).

Known as the "Third Pole", the Tibetan Plateau hosts the largest area of alpine frozen ground globally (Cuo et al., 2015; Zou et al., 2017). Compared to other frozen ground landscapes worldwide, the Tibetan Plateau has higher temperatures, thinner frozen ground layers, and unstable soil thermal conditions, making it especially sensitive to climate warming (Cheng and Wu, 2007; Luo et al., 2016). The plateau is the source for several major Asian rivers, including the Yellow, Yangtze, Salween, Mekong, Indus, and Brahmaputra Rivers, supplying water resources for over 2 billion people (Yao et al., 2022). The Yellow River, China's second-largest river, originates from the northeastern Tibetan Plateau. The source region of the Yellow River (SRYR) contributes 35% of its total runoff (Hu et al., 2011; Jin et al., 2022) and is underlain by zones of permafrost and SFG. Over recent decades, this region has experienced significant degradation of frozen ground (Luo et al., 2020; Sheng et al., 2020; Zhao et al., 2020), which threatens water resource security and poses challenges to water supply and sustainable development in downstream regions (Fang et al., 2025; Immerzeel et al., 2010; Wang et al., 2023a). Consequently, investigating the runoff response to frozen ground degradation is critically important.

There are differing viewpoints regarding the impact of frozen ground degradation on runoff. One perspective suggests that the degradation of frozen ground, accompanied by the melting of subsurface ground ice, may increase average streamflow (Walvoord and Kurylyk, 2016; Kuang et al., 2024). For instance, Li et al. (2016) indicated through isotope analysis that meltwater from permafrost ground ice contributed up to 25% of total runoff in the northeastern Tibetan Plateau, and Ma et al. (2019) estimated a potential 4.9% contribution from ground ice meltwater to river runoff in the SRYR. However, continuous warming could eventually exhaust this meltwater source, marking a critical tipping point (Gruber et al., 2017; Wang et al., 2023b). By contrast, some scholars argue that frozen ground degradation leads to a decrease in average streamflow (Cheng and Jin, 2013; Cheng and Wu, 2007; Wang, H et al., 2018). This is because the thickening of the active layer increases the soil water storage capacity, resulting in reduced runoff generation. Additionally, the increased soil moisture evaporation from the active layer depletes some of the water that would have contributed to runoff, thereby reducing the runoff ratio (Qiu, 2012; Wang, T. et al., 2018; Guo et al., 2025).

Typically, hydrological impacts of frozen ground degradation are assessed through two distinct approaches: bottom-up physical modelling and top-down statistical approaches. Physically based models incorporating water-heat coupling mechanisms have demonstrated partial success in characterizing soil freeze-thaw effects on hydrological processes (Gao et al., 2018; Zheng et al., 2018; Yi et al., 2014). However, these models face substantial challenges in accurately simulating the complex water-thermal interactions inherent to frozen soils. First, accurate quantification of phase-change latent heat fluxes and associated soil pore structure modifications during freeze-thaw transitions remain elusive due to insufficient mechanistic understanding of these processes (Gao et al., 2021; Walvoord and Kurylyk, 2016). Second, large uncertainties remain in the parameterization of soil moisture and heat fluxes in the frozen ground layer. The substantial spatial variability in frozen ground thickness, ice content, and soil types makes it difficult for current models, which largely rely on empirical parameters, to accurately represent water-thermal dynamics (Andreson et al., 2020; Harp et al., 2016; Lawrence and Slater, 2008).

In addition to physically based models, top-down statistical approaches have also been employed to investigate runoff changes. One commonly used method involves statistical analyses of the relationships between runoff, precipitation, air temperature, and indicators of frozen ground degradation over seasonal to interannual timescales (Hu et al., 2011; Ma et al., 2019). These studies typically rely on correlation analysis and trend detection to infer the hydrological impacts of permafrost degradation. Another approach is based on the Budyko framework and elasticity analysis, implicitly incorporating the landscape parameter n to quantify the relative contributions of climate and land surface change to long-term shifts in streamflow (Wang, T. et al., 2018; Wu et al., 2020; Chang et al., 2024). While statistical methods circumvent assumptions inherent in physical modelling, they predominantly focus on long-term average streamflow changes and often lack the resolution to differentiate runoff responses across various land surfaces (such as permafrost vs. SFG), unless those land surface types coincide with distinct gauged basins.

Recently, Kirchner (2022) proposed a mathematical method for estimating impulse response functions in nonlinear, nonstationary, and heterogeneous systems by combining nonlinear deconvolution and demixing techniques. Building on this foundation, ensemble rainfall-runoff analysis (ERRA) has been developed to facilitate data-driven, nonparametric, and model-independent estimation of impulse responses in hydrological systems (Kirchner, 2024). ERRA enables the quantification of nonlinear, nonstationary, and spatially heterogeneous hydrologic response directly from observational data, without the need to assume or calibrate any specific process-based model. This makes it particularly useful for comparing hydrologic behaviour before and after frozen ground degradation, enabling the assessment of how thawing permafrost alters runoff generation. ERRA complements long-term water balance studies by quantifying how runoff responds to daily or hourly variations in precipitation inputs (depending on the available data). It also allows runoff responses from different land surfaces to be distinguished and quantified, even if they are not individually gauged.

In this study, we apply ERRA to investigate the impact of frozen ground degradation on event-scale runoff response to daily precipitation in the SRYR during the period 1979–2018. We document how hydroclimate conditions and frozen ground
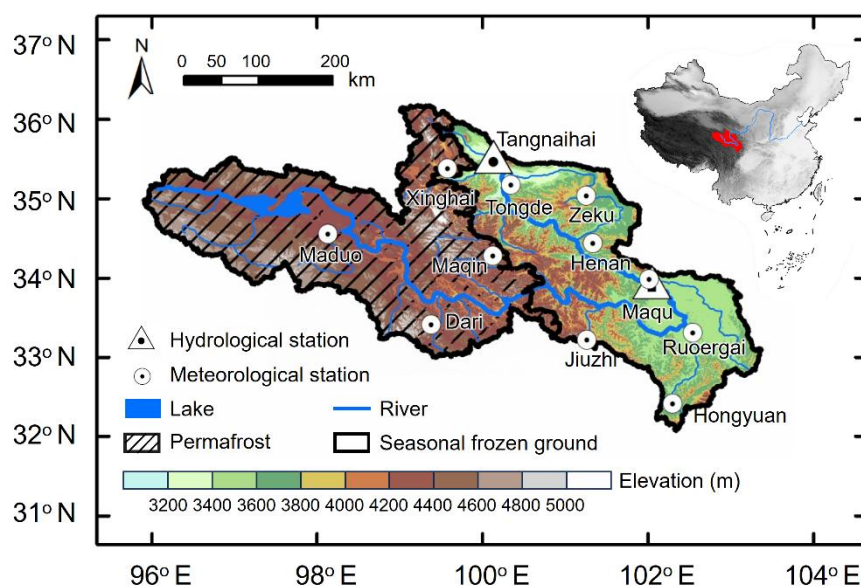
95 characteristics have changed over these four decades in the SRYR. Using ERRA, we quantify the influence of frozen ground degradation on runoff response to daily precipitation, by comparing regions underlain by permafrost and seasonally frozen ground, and we examine how this runoff response varies with precipitation intensity. Finally, we explore how permafrost degradation, as measured by changes in active layer thickness, affects runoff response to daily precipitation in the SRYR.

2 Data and methods

100 ### 2.1 Study area

The Yellow River, originating in the northeastern Tibetan Plateau, is the second-longest river in China. Its source region, referred to as the source region of the Yellow River (SRYR), is situated upstream of the Tangnaihai hydrological station (Fig.1). The SRYR spans from 95°50′E to 103°30′E and from 32°00′N to 35°40′N, with elevations ranging from 2,650 m to 6,250 m. Covering an area of approximately 123,800 km², it accounts for about 16% of the total Yellow River basin. As the

105 primary runoff-generating region, the SRYR contributes around 35% of the Yellow River's total annual runoff (Hu et al., 2011). As shown in Fig. 1, the SRYR lies within a transitional zone between continuous permafrost and seasonally frozen ground (SFG) (Zou et al., 2017), making it particularly sensitive to climate-induced permafrost degradation.

Figure 1: Location of the study area, hydrological and meteorological stations, and the distribution of permafrost and
110 **seasonally frozen ground in the source region of the Yellow River.**

2.2 Data

We obtained daily runoff observations from the Tangnaihai station, the hydrological control station of the source region of the Yellow River (SRYR), and from the Maqu station (Fig. 1). The dataset spans the period from 1979 to 2018 and was

sourced from the Annual Hydrological Reports published by the Ministry of Water Resources of China
115 (http://www.mwr.gov.cn/sj/tjgb/szygb).

Daily gauged precipitation data, collected from 11 meteorological stations (Fig. 1 and Table S1) within the SRYR for the period 1979–2018, were provided by the China Meteorological Administration (CMA) (http://data.cma.cn). In addition, we used gridded precipitation data from the China Meteorological Forcing Dataset (CMFD; Yang et al., 2019; https://data.tpdc.ac.cn/en/data/), which synthesizes data from various remote sensing products, reanalysis datasets, and
120 ground-based meteorological station data. The CMFD provides gridded data at a spatial resolution of 0.1° and a temporal resolution of 3 hours, recorded in Coordinated Universal Time (UTC+0). Since the gauged runoff, precipitation, and frozen soil depth data are recorded in UTC+8, we first converted the hourly CMFD precipitation data from UTC+0 to UTC+9 prior to daily aggregation, thereby limiting the time mismatch between daily precipitation and daily runoff to just one hour.

The observed frozen soil depth (FSD) data were collected from 9 CMA stations (Table S1). According to CMA (2007), daily
125 measurements of frozen soil depth are manually taken using a standard frozen soil apparatus, which is vertically embedded in the field. The frozen soil depth is determined by the length of ice formed inside a rubber tube, with recording starting when the soil temperature (T_s) drops below 0°C. The temporal coverage of frozen soil data varies across stations, with most providing continuous records from 1981 to 2015. In addition, we used gridded frozen ground data from the Geomorphology-Based Ecohydrological Model (GBEHM), which provides annual estimates of active layer thickness (ALT) in permafrost
130 regions and the maximum thickness of seasonally frozen ground (MTSFG) in seasonally frozen areas at a spatial resolution of 1 km for the period 1980–2018 (Wang et al., 2023a; Wang et al., 2023b). The ALT and MTSFG datasets have both been validated against in situ observations and have demonstrated good performance (Wang et al., 2023a; Wang et al., 2023b).

Leaf area index (LAI) data were derived from the GLASS-AVHRR V4.0 product (Liang et al., 2021; http://www.glass.umd.edu/Download.html), which provides 8-day data at a spatial resolution of 0.05°, covering the period
135 from 1982 to 2018. Evapotranspiration (*ET*) estimates were obtained from the GLEAM v3.8a dataset (Martens et al., 2017; https://www.GLEAM.eu/), which offers daily values at a spatial resolution of 0.25° and spans from 1980 to 2022. To estimate changes in terrestrial water storage (ΔS), we employed a reconstruction of terrestrial water storage anomalies (TWSA) based on the Gravity Recovery and Climate Experiment (GRACE). Since its launch in 2002, GRACE has proven to be a powerful tool for monitoring large-scale variations in terrestrial water storage (Kornfeld et al., 2019; Rodell and Reager,
140 2023). Here, we used the data-driven reconstruction developed by Humphrey and Gudmundsson (2019), which leverages a statistical model trained on GRACE observations to infer past climate-driven TWSA from historical and near-real-time meteorological datasets. This reconstruction provides monthly TWSA data at a spatial resolution of 0.5°, covering the period from 1979 to 2014 (https://doi.org/10.6084/m9.figshare.7670849).

2.3 Ensemble rainfall-runoff analysis

145 In this study, we employed ensemble rainfall-runoff analysis (ERRA), a data-driven and model-independent approach developed by Kirchner (2022) and Kirchner (2024), to investigate hydrological response to frozen ground degradation. In a linear, time-invariant system, the relationship between the input, the output, and the response function can be expressed using a convolution equation:

$$y(t) = \int_0^\infty \beta(\tau)\, x(t - \tau) d\tau \,, \tag{1}$$

150 where x is the input signal, y is the output signal, t is time, τ is the time lag between input and output, and $\beta(\tau)$ is the system impulse response function. In a watershed system, precipitation (P) serves as the input and runoff (Q) as the output. Using observed precipitation and runoff data, the watershed response function $\beta(\tau)$ can be inferred via deconvolution, allowing the analysis of rainfall-runoff processes based on Eq. (1).

Historically, system analysis methods have been primarily applied in engineering for approximate estimations, with limited
155 use in studies of physical hydrological processes. For computational simplicity, classical deconvolution approaches typically assume that the system is linear and stationary, as shown in Eq. (1). For example, the unit hydrograph method (Sherman, 1932) assumes that runoff response is proportional to rainfall (i.e., linear), invariant over time (stationary), and uniform across space (homogeneous). These assumptions, however, do not hold for many real-world watersheds, which often exhibit nonlinear, nonstationary, and heterogeneous behaviour.

160 To overcome these limitations, Kirchner (2022) introduced a mathematical method that combines deconvolution and demixing techniques with autoregressive moving-average (ARMA) noise correction to analyse impulse responses in noisy time series. This approach forms the basis of ERRA (Kirchner, 2024), which analyses the impulse response of hydrologic systems without invoking the unit hydrograph's assumptions of linearity, stationarity, and homogeneity. Thus, ERRA can not only quantify rainfall-runoff impulse responses, but also reveal how they vary with precipitation intensity (nonlinearity),
165 antecedent moisture conditions (non-stationarity), and watershed characteristics (heterogeneity). Thus, ERRA provides a robust framework for diagnosing hydrological responses to precipitation in frozen ground degradation regions, where system dynamics are highly variable and complex.

ERRA characterizes runoff response using Nonlinear Response Functions (NRFs), which describe how a catchment reacts to precipitation across different rainfall intensity ranges, and weighted average Runoff Response Distributions (RRDs), which
170 represent the average runoff generated per unit of precipitation at each time lag, while explicitly accounting for the underlying nonlinearity. Both NRFs and RRDs capture the time-dependent streamflow response to precipitation pulses as functions of the lag time following the rainfall event. As a data-driven and model-independent framework, ERRA quantifies catchment behaviour without making assumptions about the underlying hydrological mechanisms.

3 Hydroclimate and frozen ground changes in the SRYR

175 We analysed the long-term trends in annual air temperature (T_a), precipitation (P), runoff (Q), evapotranspiration (ET), terrestrial water storage change (ΔS), and leaf area index (LAI) across the entire source region of the Yellow River (SRYR), as presented in Table 1 and Supplementary Fig. S1. Over the period 1979–2018, air temperature exhibited a statistically significant warming trend of 0.7 °C per decade ($p < 0.001$). Annual precipitation totals also showed a significant increasing trend of 24.1 mm a^{-1} per decade ($p < 0.01$). This precipitation trend is consistent between observations from the 11

180 meteorological stations and the gridded dataset (see Supplementary Fig. S2). By contrast, annual runoff displayed a non-significant decreasing trend of -7.4 mm a^{-1} per decade ($p > 0.05$), and evapotranspiration as estimated by GLEAM increased significantly by 8.7 mm a^{-1} per decade ($p < 0.001$). Terrestrial water storage change estimated from GRACE data was zero within error (2.1 mm a^{-1} per decade, n.s.).

Table 1: Trends in annual air temperature, precipitation, runoff, evapotranspiration, water storage change and leaf
185 **area index in the SRYR for the period 1979–2018, and for the sub-periods 1979–1998 and 1999–2018.**

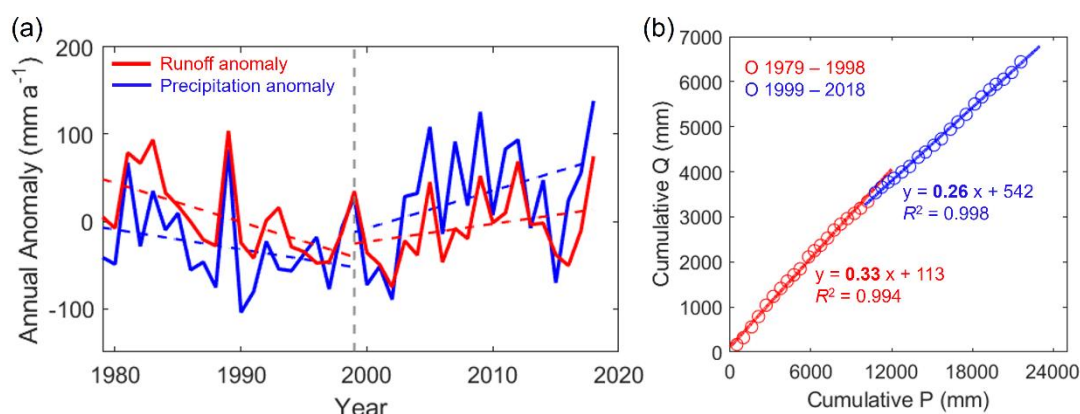|	1979–2018	1979–1998	1999–2018
T_a (°C per decade)	0.7***	0.3	0.6***
P (mm a^{-1} per decade)	24.1**	-22.7	43.3
Q (mm a^{-1} per decade)	-7.4	-44.6**	20.6
ET (mm a^{-1} per decade)	8.7***	10.6	-1.5
ΔS (mm a^{-1} per decade)	2.1	-0.4	4.2
LAI (m^2 m^{-2} per decade)	0.049***	0.026	0.027**

Note: *, **, and *** denote significance levels of $p < 0.05$, $p < 0.01$, and $p < 0.001$, respectively.

The interannual variations in runoff appear to be linked to variations in precipitation and evapotranspiration (Fig. 2a and Table 1). During the first 20 years (1979–1998), precipitation decreased by -22.7 mm a^{-1} per decade (n.s.) and evapotranspiration (estimated by GLEAM) increased by 10.6 mm a^{-1} per decade (n.s.), both contributing to a significant

190 decline in runoff of -44.6 mm a^{-1} per decade ($p < 0.01$). During the second 20 years (1999–2018), all of these trends reversed (but were statistically non-significant), with precipitation increasing by 43.3 mm a^{-1} per decade (n.s.), evapotranspiration decreasing by -1.5 mm a^{-1} per decade (n.s.), and runoff increasing by 20.6 mm a^{-1} per decade (n.s.). Changes in water storage (estimated from GRACE data) were small; they averaged -0.4 mm a^{-1} and exhibited no trend (-0.4 mm a^{-1} per decade, n.s.) in the first period; in the second period, they averaged 3.8 mm a^{-1} and grew by 4.2 mm a^{-1} per decade (n.s.).

195 Figure 2b illustrates the double-mass curves of precipitation versus runoff for the SRYR. During the first 20-year period (1979–1998), the runoff ratio (Q/P), represented by the slope of the regression line, is 0.33, whereas in the subsequent 20 years (1999–2018), it decreased to 0.26. This decline in the runoff ratio indicates a shift in the precipitation-runoff

relationship since 1998, suggesting that less runoff was generated per unit of precipitation. Such changes in the double-mass curves can be attributed to rising air temperatures and the associated alterations in terrestrial water storage dynamics.

Figure 2: Changes in precipitation and runoff in the source region of the Yellow River (SRYR) during 1979-2018. (a) Catchment-averaged annual anomalies of precipitation and runoff for the SRYR during 1979–2018; dashed lines indicate linear trends before and after 1999. Annual anomalies in runoff are strongly correlated with anomalies in precipitation, but somewhat damped. (b) Double-mass curves of precipitation versus runoff for the SRYR, with straight lines representing the corresponding linear regression fits. The runoff ratio is distinctly lower in 1999–2018 compared to 1979–1998.

We then analysed the interannual variability of frozen soil depth (FSD; Fig. 3 and Supplementary Fig. S3) using FSD observations from nine China Meteorological Administration stations. Among these stations, four (Maduo, Dari, Maqin, and Xinghai) are located in permafrost regions of the SRYR, where FSD measurements represent the depth of seasonal freezing within the active layer. The remaining five stations (Henan, Jiuzhi, Maqu, Ruoergai, and Hongyuan) are situated in areas characterized by seasonally frozen ground (as shown in Fig. 1).
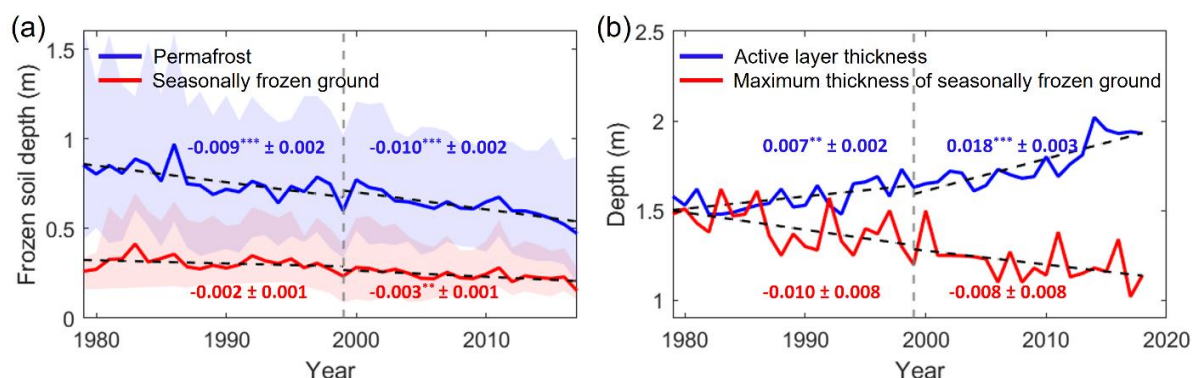
In Fig. 3a, the blue line shows the time series of the annual maximum FSD across the permafrost region (averaged over the four permafrost stations), while the red line shows the corresponding time series for the seasonally frozen ground region (averaged over the five seasonally frozen ground stations). The shaded areas around each line indicate the range of FSD values observed at individual stations within each group. The analysis reveals a clear decreasing trend in FSD at the permafrost stations, with an average rate of approximately -0.1 m per decade ($p < 0.001$) during the period 1979–2018. By contrast, a more moderate decline is observed at the seasonally frozen ground stations, with an average rate of about -0.03 m per decade ($p < 0.001$). This pattern is also evident in Supplementary Fig. S3, where a substantial difference is observed between the mean annual FSDs of the first 20 years (1979–1998) and the last 20 years (1999–2018) at the permafrost stations. In comparison, the seasonally frozen ground stations show relatively little change in average FSD between the two periods. Regional frozen ground degradation was also estimated from GBEHM simulations. In permafrost regions, GBEHM estimates of annual maximum active layer thickness (ALT) exhibited a continuous increasing trend, with the rate rising from 0.07 m per decade during 1979–1998 to 0.18 m per decade during 1999–2018. Consistent with this gradual increase in thaw

depth in the permafrost regions, the maximum freezing depth in the seasonally frozen ground regions (maximum thickness
of seasonally frozen ground MTSFG, estimated by GBEHM) declined over the two periods, at average rates of roughly -0.09
225 m per decade.

The trends outlined here demonstrate ongoing degradation of permafrost and seasonally frozen ground over the four-decade
period of record, and also document trends in precipitation and streamflow. From the trends alone, however, one cannot test
whether the coupling between precipitation and streamflow has changed, as might be expected from widespread degradation
of frozen ground in the SRYR. In the following sections, we use ensemble rainfall-runoff analysis (ERRA) to quantify the
230 coupling between daily variations in precipitation and streamflow, and assess how that coupling has changed over time as
frozen ground degradation has progressed.

Figure 3: Trends in permafrost and seasonally frozen ground in the source region of the Yellow River. (a) Interannual
variation from 1979 to 2018 in the mean frozen soil depth at four permafrost stations (blue line) and five seasonally frozen
235 ground stations (red line). Shaded areas represent the range of values observed across individual stations within each group.
Dashed black lines indicate linear trends (m a^{-1}) for the periods 1979–1998 and 1999–2018; *, **, and *** denote $p < 0.05$, $p < 0.01$, and $p < 0.001$, respectively. Average trends are significant in both regions and both periods, but rates of frozen ground
degradation are distinctly faster in the permafrost region. (b) Averages of annual maximum active layer thickness in the
permafrost region (blue line) and annual maximum freezing depth in the seasonally frozen ground region (red line) from
240 1979 to 2018, derived from GBEHM model simulation. Active layer thickness shows increasing trends that accelerate in the
second 20-year period. Trends in maximum thickness of seasonally frozen ground are more uncertain due to year-to-year
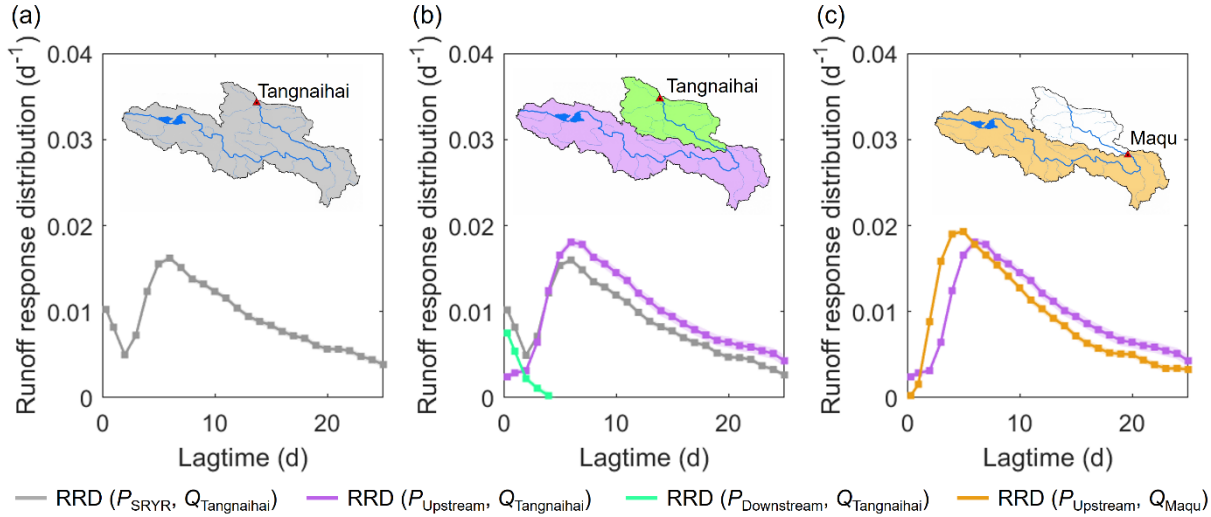variations in the model simulations.

4 Effect of frozen ground degradation on runoff response

4.1 Runoff response in the SRYR and its upstream and downstream basins

245 The nonlinear, nonstationary, and spatially heterogeneous hydrological response of the SRYR to daily precipitation can be
effectively characterized using response distributions derived from ERRA (see Methods in Sect. 2.3). As illustrated in Fig.
4a, the runoff response distribution (RRD), calculated with gridded precipitation as the input, depicts how runoff response
per unit precipitation is distributed over time. Figure 4a exhibits a marked double peak, with a first peak occurring the same
day as precipitation, and the second peak arriving after a lag of approximately six days. To explore the origins of this double

250   peak, we calculated precipitation rates separately for the basin upstream and downstream of Maqu, and then used ERRA to deconvolve streamflow at the basin outlet by both precipitation sources jointly.
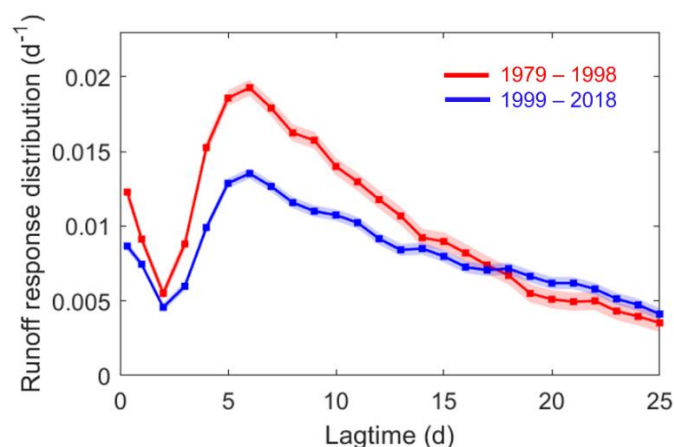

Figure 4: Panel (a) shows the runoff response distribution (RRD) calculated by deconvolving Tangnaihai streamflow using precipitation averaged over the entire source region of the Yellow River for 1979–2018 (grey line). The shaded areas
255   represent one standard error (where these are larger than the plotting symbols). Panel (b) shows that the double-peak behaviour of the RRD in panel (a), also reproduced here in grey, can be explained as the sum of the runoff response to precipitation falling downstream of Maqu (green line and green basin in map) and upstream of Maqu (purple line and purple basin in map). The green and purple lines are calculated by ERRA's deconvolution and demixing approach, which simultaneously deconvolves the streamflow at Tangnaihai by precipitation in the upper basin and precipitation in the lower
260   basin. The first peak mostly reflects runoff response to lower-basin precipitation, and the second peak mostly reflects runoff response to upper-basin precipitation. Panel (c) compares the runoff response of streamflow at Tangnaihai to precipitation upstream of Maqu (purple line from panel b, reproduced here) and the runoff response of streamflow at Maqu, inferred by ERRA from precipitation upstream of Maqu and streamflow measured at Maqu (yellow line). The purple line has a similar shape to the RRD at Maqu (yellow line), but is lagged by 1-2 days, consistent with propagation of hydrological signals along
265   the ~300 km channel between Maqu and Tangnaihai at a celerity of roughly 6-12 km h^{-1}.

The grey curve in Fig. 4a shows the RRD based on all precipitation events during the period 1979–2018. In response to a unit precipitation input, runoff at the catchment outlet initially peaks at approximately 0.01 d^{-1} within the same day, followed by a gradual decline over the next few days. The RRD then rises again to a second, higher peak of approximately 0.016 d^{-1} around the sixth day, after which it recedes. This double-peak pattern is further explored in Fig. 4b, which shows how

270   streamflow at Tangnaihai responds to precipitation in the upper and lower basins of the SRYR (upstream and downstream of Maqu, i.e., relatively far from, and relatively close to, the outlet at Tangnaihai). The purple and green lines in Fig. 4b are estimated by using ERRA's deconvolution and demixing capabilities to deconvolve streamflow at Tangnaihai by precipitation in both the upper and lower basins jointly (see Sect.2 of Kirchner, 2024 for details). As Fig. 4b shows, the first peak mostly reflects runoff generation downstream from Maqu (and thus close to the outlet at Tangnaihai; the green line),

275   and the second peak mostly reflects runoff generated upstream from Maqu (and farther from the outlet; the purple line). Runoff generated upstream from Maqu dominates the runoff response at Tangnaihai, because the upper basin comprises over

two-thirds of the total drainage area. As a check on the plausibility of the deconvolution and demixing approach used in Fig. 4b, Fig. 4c compares the runoff response at Tangnaihai to precipitation upstream of Maqu (purple line) and the runoff response at Maqu to the same precipitation (yellow line). The two response curves are broadly similar, but with a phase shift

280 of 1-2 days that is consistent with propagation of the hydrological response from Maqu to Tangnaihai at a celerity of approximately 6-12 km h^{-1}, which is broadly consistent with celerity values measured in other rivers of similar size (Meyer et al., 2018).
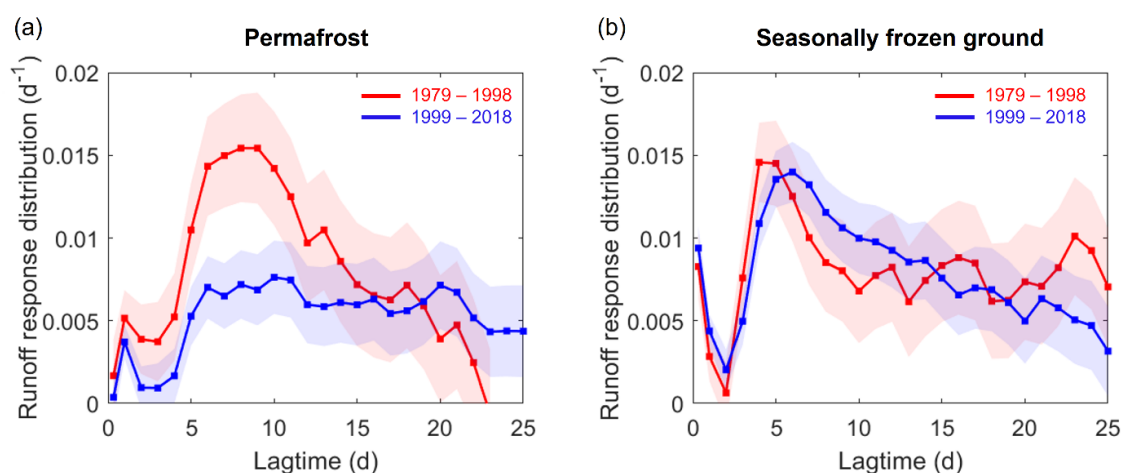

Figure 5: Runoff Response Distribution (RRD) calculated by deconvolving Tangnaihai streamflow using regionally
285 **averaged precipitation across the entire source region of the Yellow River for 1979–1998 (red line) and 1999–2018**
(blue line). The shaded areas around the lines represent error bars, indicating one standard error. Runoff response per unit precipitation decreases substantially between the first and second periods, although the lag times remain similar.

Figure 5 compares runoff response distributions at Tangnaihai (similar to Fig. 4a) for the two periods 1979–1998 and 1999–2018, as shown by the red and blue curves, respectively. A clear difference is observed between the two periods. The RRD

290 for 1979–1998 is distinctly higher than that for 1999–2018 for lags up to ~15 days, indicating a stronger overall runoff response in the first two decades. Although the timing of the main (second) peak differs by less than one day between the two periods, its magnitude decreases significantly from 0.019 d^{-1} in 1979–1998 to 0.013 d^{-1} in 1999–2018. The area under each RRD curve represents the total runoff generated per unit precipitation input, which corresponds to the average event runoff coefficient for the 25-day range of lag times analysed here. This coefficient decreases from 0.31 in the first period to

295 0.25 in the second, consistent with the results shown in Fig. 2b (average runoff coefficients of 0.33 and 0.26 for the first and second periods, respectively). These findings suggest that, for the same amount of precipitation, the catchment's capacity to generate runoff has declined in recent decades. In the next two sections, we explore whether this reduction in runoff generation capacity could be the result of frozen ground degradation in the permafrost and/or seasonally frozen ground regions of the SRYR.

4.2 Contrasting runoff responses in permafrost versus seasonally frozen ground

A central focus of this study concerns whether the observed hydrological trends outlined in Sect. 4.1 can be linked to ongoing frozen ground degradation across the SRYR. Because the hydrological effects of frozen ground degradation could differ between the permafrost and seasonally frozen ground regions (as depicted in Fig. 1), we seek to quantify how runoff response in each of these regions has changed over time. The permafrost and seasonally frozen ground regions do not follow basin boundaries, so gauging stations do not measure runoff from each region separately. Instead, runoff signals from both regions are combined in the streamflow observed at Tangnaihai. The challenge, then, is to separate these signals. This can be accomplished using ERRA's deconvolution and demixing methods analogously to Sect. 4.1, but here we jointly analyse the effects of precipitation in the permafrost and seasonally frozen ground regions, rather than in the basins upstream and downstream of Maqu (as shown in Fig. 4b).
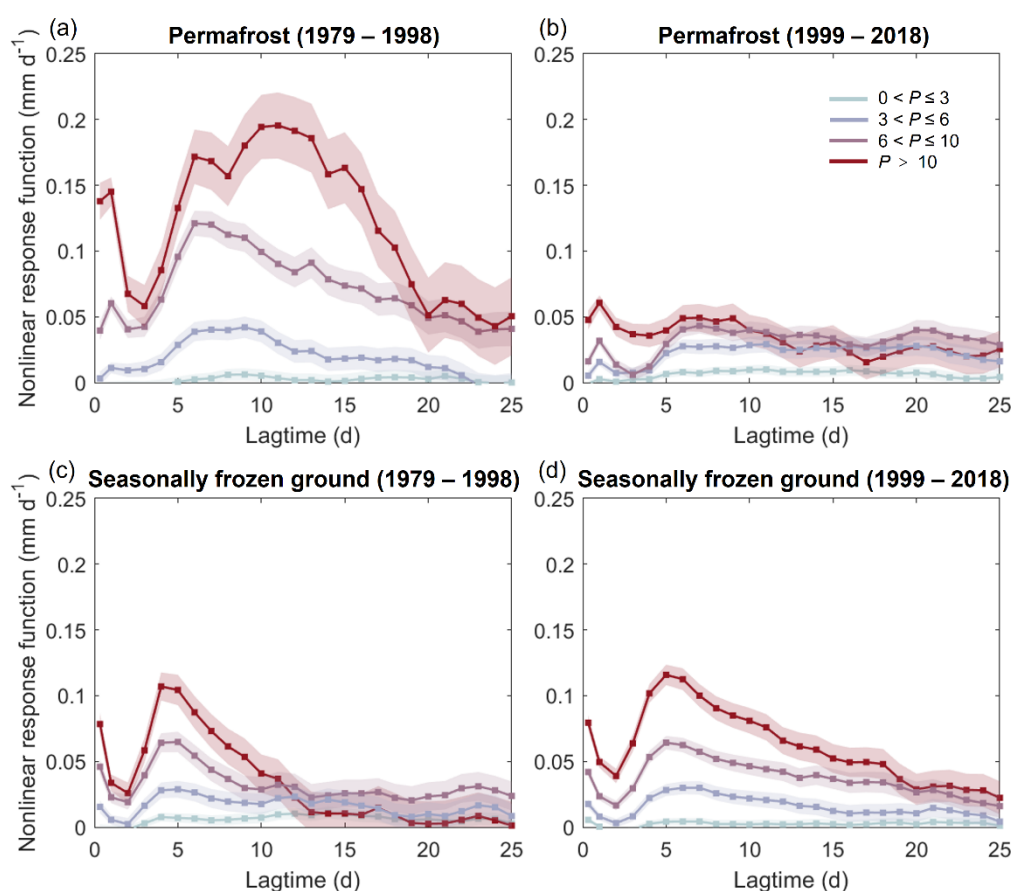

Figure 6: Weighted average Runoff Response Distribution (RRD) calculated by deconvolving Tangnaihai streamflow with joint precipitation inputs from the (a) permafrost region and (b) seasonally frozen ground region for the periods 1979–1998 (red lines) and 1999–2018 (blue lines). Shaded areas around the lines indicate one standard error. Peak runoff per unit precipitation and runoff coefficient decreased substantially between the first and second periods in the permafrost region, but remained largely unchanged in the seasonally frozen ground region.

Our analysis reveals a pronounced attenuation in the runoff response within the permafrost region between 1979–1998 and 1999–2018 (Fig. 6). During the first 20 years (1979–1998), the weighted average RRD peaks between days 6 and 10, reaching a value of ~0.015 d^{-1}, and the 25-day runoff coefficient is 0.19. However, in the subsequent 20 years (1999–2018), the timing of the RRD peak becomes much less distinct and the peak value decreases to ~0.008 d^{-1}, with the runoff coefficient declining to 0.13. In the seasonally frozen ground region, by contrast, the RRDs in the two periods have largely overlapping ranges of uncertainty, with the 25-day runoff coefficient remaining nearly constant at ~0.20.

The weighted average RRDs shown in Fig. 6 describe how runoff at Tangnaihai responds to a unit of precipitation in the permafrost and seasonally frozen ground regions. To further analyze how runoff responds to varying precipitation intensities,

we used ERRA's nonlinear response function (NRF), which quantifies runoff response over time to lagged precipitation
325 inputs in given ranges of precipitation intensity. As shown in Fig. 7, runoff response is generally greater when precipitation
intensity (here, the daily precipitation rate) is higher. For instance, in Fig. 7a, when the precipitation intensity in the
permafrost region is 0–3 mm d^{-1}, the NRF peaks at ~0.01 mm d^{-1} around day 9. However, when precipitation intensity
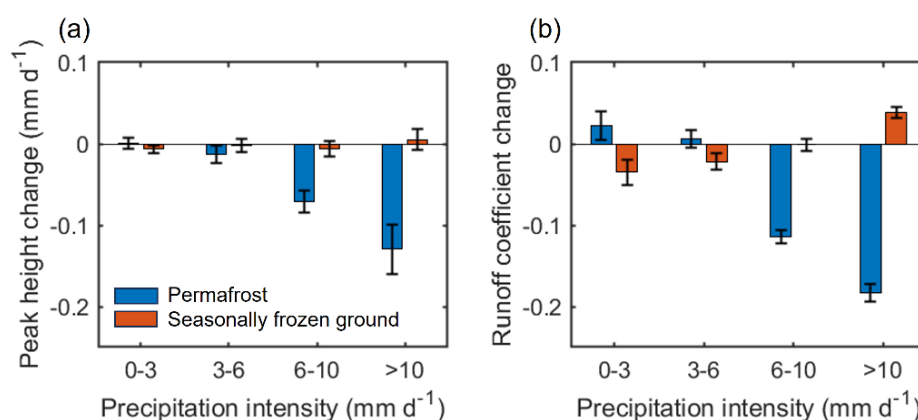increases to >10 mm d^{-1}, the NRF peaks at ~0.20 mm d^{-1} around day 11.

Figure 7: Hydrological response to different precipitation intensities quantified by Nonlinear Response Functions (NRF),
derived by deconvolving Tangnaihai streamflow by precipitation inputs in both the permafrost and seasonally frozen ground
regions simultaneously. The coloured lines represent different precipitation intensities, and the shaded areas around the lines
indicate one standard error. The decline in the NRFs between the first and second 20-year periods becomes more pronounced
at higher precipitation intensities in the permafrost region, but exhibits much smaller changes in the seasonally frozen ground
335 region.

Comparing the NRFs in the permafrost region during the first 20 years (1979–1998; Fig. 7a) and the subsequent 20 years
(1999–2018; Fig. 7b) reveals substantial changes. Notably, the decline in the NRFs between the two periods becomes more
pronounced at higher precipitation intensities. For example, under low precipitation intensity (0–3 mm d^{-1}), the NRF peak
height in 1999–2018 is only slightly lower than in 1979–1998, showing a marginal decrease of 0.001 ± 0.006 mm d^{-1}. But in
340 the highest range of precipitation intensity (>10 mm d^{-1}), the peak height declines by 0.13 ± 0.03 mm d^{-1}, as illustrated by the

13

blue bars in Fig. 8a. A similar pattern is observed in the 25-day runoff coefficients: when precipitation intensity is 0–3 mm d⁻¹, the runoff coefficient changes by only 0.02 ± 0.02 between the two periods, but at precipitation intensities of >10 mm d⁻¹, the runoff coefficient decreases by 0.2 ± 0.01 (Fig. 8b). In contrast to the dramatic changes in the hydrological behaviour of the permafrost region, the seasonally frozen ground region exhibits much smaller changes over the same time periods (Figs.

345 7c and 7d), with both the NRF peak height and the runoff coefficient remaining relatively stable (Fig. 8).

Figure 8: Changes in (a) the peak height of the Nonlinear Response Function (NRF) and (b) the 25-day runoff coefficient derived by deconvolving Tangnaihai streamflow by different ranges of precipitation intensities between 1979–1998 and 1999–2018, in the permafrost region (blue bars) and the seasonally frozen ground region (red bars). The black error bars
350 indicate one standard error. In the permafrost region, the largest decreases in NRF peak height and runoff coefficient are observed at the highest precipitation intensities. In the seasonally frozen ground region, changes in NRF peak height and runoff coefficient are small and statistically insignificant at all precipitation intensities.

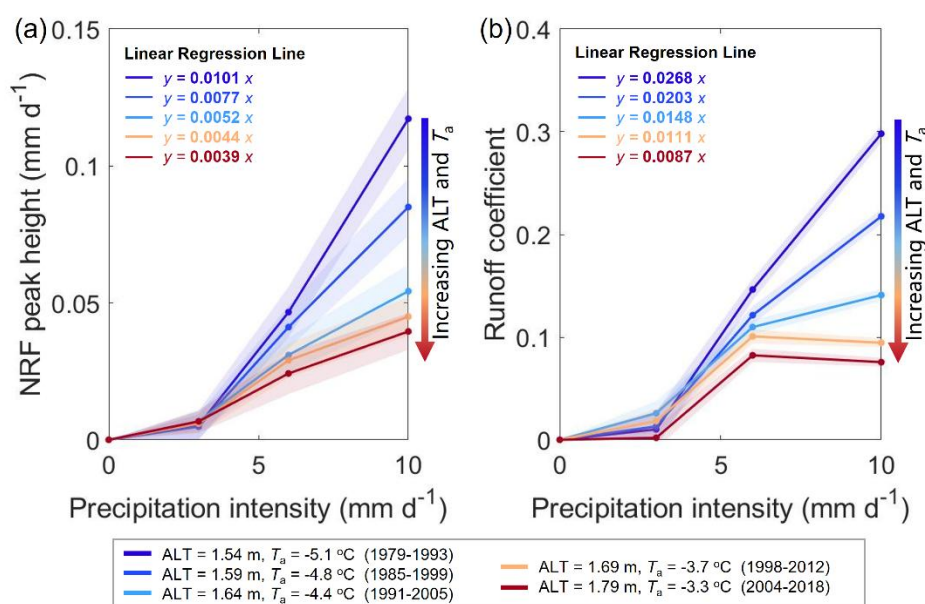**4.3 Runoff responses under different levels of permafrost degradation**

To further investigate the runoff sensitivity to precipitation following permafrost degradation, we employed a moving
355 window approach to divide the 40-year dataset into overlapping 15-year intervals, with a 6-year step between consecutive windows. This approach yielded five time periods, as indicated by the different coloured lines in Fig. 9. For each interval, we computed the mean annual active layer thickness (ALT) and air temperature (T_a) to quantify the extent of permafrost degradation. We then applied the ERRA framework, following the same methodology as applied in Fig. 7, to assess the nonlinear runoff response under varying precipitation intensities across these time periods. Specifically, we examined
360 changes in the peak height of the Nonlinear Response Functions (NRF; Fig. 9a) and the 25-day runoff coefficient (Fig. 9b) across the five time intervals.

As air temperature rises and the active layer becomes thicker (from blue line to red line), both the NRF peak height (Fig. 9a) and the 25-day runoff coefficient (Fig. 9b) show a marked decline. This pattern is especially pronounced under high precipitation intensity (6–10 mm d⁻¹). In such conditions, as ALT increases, the NRF peak height drops significantly from
365 0.12 mm d⁻¹ (first 15 years, 1997–1993) to 0.04 mm d⁻¹ (last 15 years, 2004–2018), and the runoff coefficient decreases from 0.30 to 0.08. By contrast, under low precipitation intensity (0–3 mm d⁻¹), changes in the NRF peak height and runoff

coefficient are minimal, with peak height varying by only around 0.002 mm d⁻¹ and the runoff coefficient varying by approximately 0.05. These changes are reflected in the slopes of the linear regression lines between NRF peak height and precipitation intensity, as well as between the runoff coefficient and precipitation intensity. The slope of the regression line between NRF peak height and precipitation intensity is ~0.01 when the mean annual ALT is 1.54 m and T_a is -5.1 °C (first 15 years, 1997–1993). However, as the mean annual ALT increases to 1.79 m and Ta increases to -3.3 °C (last 15 years, 2004–2018), the slope of the regression line decreases to ~0.004. Similarly, for the runoff coefficient and precipitation intensity, the slopes of the fitted lines decrease from ~0.027 to ~0.009 as ALT and T_a increases.

Figure 9: (a) Peak height and (b) 25-day runoff coefficient estimated by the Nonlinear Response Function (NRF) for Tangnaihai streamflow as functions of precipitation intensity under different active layer thicknesses and average air temperatures in the permafrost region, for overlapping 15-year periods. Coloured circles represent results calculated by ERRA during different periods, and the shaded areas around the lines indicate one standard error. Increases in active layer thickness (from blue to red lines) are associated with dramatic decreases in the sensitivity of peak height and runoff coefficient to precipitation intensity.

4 Discussion

Recent studies have reported contrasting trends between precipitation and runoff in the source region of the Yellow River (Ma et al., 2019; Meng et al., 2016; Wang, T. et al., 2018; Wu et al., 2020). Despite a statistically significant increase in precipitation over recent decades, runoff in the region has shown a slight but statistically insignificant decreasing trend (Table 1 and Fig. 2). At the same time, observational data provide clear evidence of frozen ground degradation across the SRYR (Fig. 3). Several modelling approaches that incorporate coupled water and heat fluxes have emphasized the role of frozen ground degradation in influencing hydrological responses in the SRYR (Qin et al., 2017; Song et al., 2024; Wang et

al., 2023a; Yang et al., 2023). Model simulations indicate that frozen ground degradation may lead to the release of meltwater from frozen soils, increased soil water storage capacity and moisture content, and enhanced groundwater storage, which combine to reduce surface runoff. However, these model simulations often rely on uncertain assumptions and parameterizations, and lack observational validation of internal processes, thereby raising concerns about their reliability (Gao et al., 2021; Lawrence and Slater, 2008; Walvoord and Kurylyk, 2016).
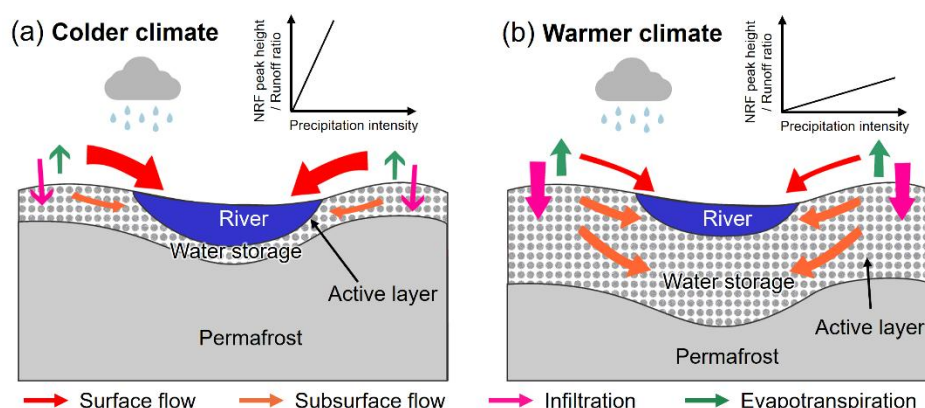
The analysis presented above provides new observational constraints on the hydrological effects of frozen ground degradation in the permafrost and seasonally frozen ground regions of the SRYR. Figure 4 reveals that the SRYR exhibits double-peak runoff response, with the first peak generated mostly in the lower basin close to the outlet, and the second, broader peak generated in the upper basin farther from the outlet. This demonstrates that streamflows originating in different parts of the SRYR have distinct signatures that can be detected at the basin outlet and can be demixed from signals generated in other parts of the basin. This deconvolution and demixing approach allow us to infer how runoff responds to precipitation in different parts of the basin, even if they are not individually gauged. This capability of ERRA is particularly valuable to distinguish the hydrological effects of frozen ground degradation between the permafrost and seasonally frozen ground (SFG) regions. The permafrost and SFG regions do not align with hydrological basin boundaries (as shown in Fig. 1), and existing gauging stations (such as Tangnaihai and Maqu) do not measure runoff from each region separately. Instead, runoff signals from both regions are combined in the streamflow observed at Tangnaihai. Consequently, it is challenging to separate the runoff response from each frozen ground type using conventional methods. ERRA addresses this limitation by jointly analysing the effects of precipitation in the permafrost and SFG regions on the outlet runoff. As shown in Fig. 6, this approach enables the separation of overlapping runoff signals at the basin outlet from permafrost and SFG regions. The results reveal that peak runoff per unit precipitation declined substantially between the first and second 20-year periods in the permafrost region, whereas it remained largely stable in the SFG region.

One of the most important contributions of ERRA to understanding runoff responses to frozen ground degradation lies in its ability to assess runoff behaviour under varying precipitation intensities, as reflected in the Nonlinear Response Function (NRF) (Figs. 7 and 8). During the earlier period (1979–1998), when the permafrost region was underlain by a thick frozen impermeable layer, higher precipitation intensities were associated with distinctly higher NRF peak heights, greater total runoff (represented by the area under the NRF curve), and elevated 25-day runoff coefficients (Fig. 7a). This strong sensitivity of runoff response to precipitation intensity suggests that the thick permafrost limited infiltration capacity, leading to reduced infiltration and consequently increased surface runoff generation. However, in the later period (1999–2018), both the NRF peak height and runoff coefficient in the permafrost region decreased substantially compared to the earlier period (Figs. 7b and 8), and became much less sensitive to differences in precipitation intensity. Specifically, for precipitation intensities exceeding 10 mm d^{-1}, the NRF peak height and 25-day runoff coefficient declined by 73% and 72%, respectively, between the two periods. This shift is consistent with enhancement of soil porosity, hydraulic connectivity, and water storage

420   capacity following permafrost degradation (Cheng and Jin, 2013; Ma et al., 2019; Shi et al., 2020; Wang et al., 2023a). As a result, more precipitation infiltrates into the soil before surface runoff is generated, with runoff occurring only once the upper soil layers reach saturation (as shown in Fig. 10b). Thus, runoff response becomes less sensitive to increasing precipitation intensity, as illustrated in Figs. 7b and 8. The shift in active layer thickness implies that infiltration-excess mechanisms are likely to have played a smaller role in runoff generation during the second two decades of record than during the first two

425   decades (Fig. 10a).

With ongoing climate warming, the active layer thickness has been gradually increasing, which enhances the soil water storage capacity of the watershed. As a result, both peak runoff (Fig. 9a) and total runoff volume (Fig. 9b) have declined. These changes carry important implications for water resource management in permafrost regions under future climate change scenarios. Specifically, the continued thickening of the active layer suggests that surface water availability may

430   further decrease in these regions, potentially intensifying drought risks. On the other hand, the increased soil water retention capacity also strengthens the system's buffering effect, making it more difficult for extreme precipitation events to generate large flood peaks. Consequently, the risk of flooding may be reduced. This dual impact highlights the necessity of balancing drought mitigation and flood risk assessment in future hydrological planning for permafrost-affected areas.

435   **Figure 10: Hydrological response to frozen ground degradation under (a) colder and (b) warmer climate conditions.**

5 Conclusion

In this study, we used ensemble rainfall-runoff analysis (ERRA) to investigate the impacts of frozen ground degradation on runoff responses in the source region of the Yellow River (SRYR). We first examined hydroclimatic and frozen ground changes across the basin. Despite a statistically significant increase in precipitation in recent decades, regional runoff

440   exhibited a slight but statistically insignificant decreasing trend (Fig. 2, Table 1). Meanwhile, observational data indicated widespread degradation of frozen ground throughout the SRYR (Fig. 3). We employed ERRA to assess the effects of frozen ground degradation on runoff dynamics. The results show that in the permafrost zone, the peak runoff response during 1999–

17

2018 declined by 47%, and the 25-day runoff coefficient decreased by 32% compared to the period 1979–1998 (Figs. 5 and

6). By contrast, no significant changes were observed in the seasonally frozen ground (SFG) zone (Fig. 6). The reductions in

445 runoff response were especially pronounced under higher precipitation intensities. When daily precipitation exceeded 10 mm

d^{-1}, the peak runoff response declined by 73%, and the 25-day runoff coefficient dropped by 72% between the two periods

(Figs. 7–9). These shifts are attributed to increased soil porosity, improved hydraulic connectivity, and enhanced water

storage capacity within the thawed active layer, which facilitate greater infiltration and delay surface runoff generation. Our

findings highlight how permafrost degradation can fundamentally alter runoff generation processes. These insights are

450 critical for informing water resource management, drought mitigation, and flood risk assessment in cold-region basins under

ongoing climate warming.

Data availability

Daily runoff observations at the Tangnaihai station and corresponding drainage area information are available from the

Ministry of Water Resources of the People's Republic of China (http://www.mwr.gov.cn/sj/tjgb/szygb). Daily precipitation

455 and frozen soil depth data from 11 meteorological stations were obtained from the National Meteorological Information

Center of the China Meteorological Administration (http://data.cma.cn). The China Meteorological Forcing Dataset (CMFD)

is available from the National Tibetan Plateau/Third Pole Environment Data Center (Yang et al., 2019;

https://data.tpdc.ac.cn/en/data/). Gridded frozen ground data were derived from the Geomorphology-Based Ecohydrological

Model (GBEHM) (Wang et al., 2023a; Wang et al., 2023b). Leaf area index data were sourced from the GLASS-AVHRR

460 V4.0 product (Liang et al., 2021; http://www.glass.umd.edu/Download.html). Evapotranspiration data were obtained from

the GLEAM v3.8a dataset (Martens et al., 2017; https://www.GLEAM.eu/). The reconstruction of climate-driven terrestrial

water storage changes was derived from Humphrey and Gudmundsson (2019; https://doi.org/10.6084/m9.figshare.7670849).

The spatial distribution of permafrost and seasonally frozen ground was obtained from Zou et al. (2017).

Author contribution

465 Zhuoyi Tu designed the research framework, conducted the primary data analysis, and led the manuscript writing. James

Kirchner co-designed the research framework, advised on the use of ERRA, experimental design, and data analysis, and

made major contributions to the manuscript. Yuting Yang, Taihua Wang, and Juntai Han contributed key datasets, including

streamflow, meteorological, and frozen soil observations, and participated in manuscript preparation. Their regional

expertise also informed the study design and interpretation. Hansjörg Seybold, Shaozhen Liu, and Cansu Culha provided

470 technical guidance on the use of ERRA and offered suggestions for designing control experiments. All authors reviewed and

approved the final version of the manuscript.

Competing interests

The authors declare that they have no conflict of interest.

Financial support

References

480   Andresen, C. G., Lawrence, D. M., Wilson, C. J., McGuire, A. D., Koven, C., Schaefer, K., et al.: Soil moisture and hydrology projections of the permafrost region-a model intercomparison, The Cryosphere, 14, 445–459, https://doi.org/10.5194/tc-14-445-2020, 2020.

Biskaborn, B. K., Smith, S. L., Noetzli, J., Matthes, H., Vieira, G., Streletskiy, D. A., and Lantuit, H.: Permafrost is warming at a global scale, Nat. Commun., 10, 264, https://doi.org/10.1038/s41467-018-08240-4, 2019.

485   Chang, Y., Ding, Y., Zhang, S., Zhao, Q., Jin, Z., Qin, J., and Shangguan, D.: Quantifying the response of runoff to glacier shrinkage and permafrost degradation in a typical cryospheric basin on the Tibetan Plateau, Catena, 242, 108124, https://doi.org/10.1016/j.catena.2024.108124, 2024.

Cheng, G. and Jin, H.: Permafrost and groundwater on the Qinghai–Tibet Plateau and in northeast China, Hydrogeol. J., 21, 5, https://doi.org/10.1007/s10040-012-0927-2, 2013.

490   Cheng, G. and Wu, T.: Responses of permafrost to climate change and their environmental significance, Qinghai–Tibet Plateau, J. Geophys. Res.-Earth, 112, https://doi.org/10.1029/2006JF000631, 2007.

CMA (China Meteorological Administration): Specifications for Surface Meteorological Observation, Part 14: Measurement of Frozen Soil, China Meteorological Press, Beijing, China, 3 pp., 2007 (in Chinese).

Cohen, J., Screen, J. A., Furtado, J. C., Barlow, M., Whittleston, D., Coumou, D., and Jones, J.: Recent Arctic amplification
495   and extreme mid-latitude weather, Nat. Geosci., 7, 627–637, https://doi.org/10.1038/ngeo2234, 2014.

Cuo, L., Zhang, Y., Bohn, T. J., Zhao, L., Li, J., Liu, Q., and Zhou, B.: Frozen soil degradation and its effects on surface hydrology in the northern Tibetan Plateau, J. Geophys. Res.-Atmos., 120, 8276–8298, https://doi.org/10.1002/2015JD023193, 2015.

500 Fang, P., Wang, T., Yang, D., Yang, J., and Tang, L.: Permafrost degradation and concomitant hydrological changes dominated by anthropogenic greenhouse gas emissions in the Northeastern Tibetan Plateau, Geophys. Res. Lett., 52, e2024GL113679, https://doi.org/10.1029/2024GL113679, 2025.

Frauenfeld, O. W. and Zhang, T.: An observational 71-year history of seasonally frozen ground changes in the Eurasian high latitudes, Environ. Res. Lett., 6, 044024, https://doi.org/10.1088/1748-9326/6/4/044024, 2011.

Gao, B., Yang, D., Qin, Y., Wang, Y., Li, H., Zhang, Y., and Zhang, T.: Change in frozen soils and its effect on regional
505 hydrology, upper Heihe basin, northeastern Qinghai–Tibetan Plateau, The Cryosphere, 12, 657–673, https://doi.org/10.5194/tc-12-657-2018, 2018.

Gao, H., Wang, J., Yang, Y., Pan, X., Ding, Y., and Duan, Z.: Permafrost hydrology of the Qinghai–Tibet Plateau: A review of processes and modeling, Front. Earth Sci., 8, 576838, https://doi.org/10.3389/feart.2020.576838, 2021.

Gruber, S., Fleiner, R., Guegan, E., Panday, P., Schmid, M. O., Stumm, D., and Zhao, L.: Inferring permafrost and
510 permafrost thaw in the mountains of the Hindu Kush Himalaya region, The Cryosphere, 11, 81–99, https://doi.org/10.5194/tc-11-81-2017, 2017.

Guo, L., Wang, G., Song, C., Sun, S., Li, J., Li, K., et al.: Hydrological changes caused by integrated warming, wetting, and greening in permafrost regions of the Qinghai-Tibetan Plateau, Water Resour. Res., 61, e2024WR038465, https://doi.org/10.1029/2024WR038465, 2025.

515 Harp, D. R., Atchley, A. L., Painter, S. L., Coon, E. T., Wilson, C. J., Romanovsky, V. E., and Rowland, J. C.: Effect of soil property uncertainties on permafrost thaw projections: a calibration-constrained analysis, The Cryosphere, 10, 341–358, https://doi.org/10.5194/tc-10-341-2016, 2016.

Hjort, J., Streletskiy, D., Doré, G., Wu, Q., Bjella, K., and Luoto, M.: Impacts of permafrost degradation on infrastructure, Nat. Rev. Earth Environ., 3, 24–38, https://doi.org/10.1038/s43017-021-00247-8, 2022.

520 Hu, Y., Maskey, S., Uhlenbrook, S., and Zhao, H.: Streamflow trends and climate linkages in the source region of the Yellow River, China, Hydrol. Process., 25, 3399–3411, https://doi.org/10.1002/hyp.8069, 2011.

Humphrey, V. and Gudmundsson, L.: GRACE-REC: A reconstruction of climate-driven water storage changes over the last century, Earth Syst. Sci. Data, 11, 1153–1170, https://doi.org/10.5194/essd-11-1153-2019, 2019.

Immerzeel, W. W., Van Beek, L. P., and Bierkens, M. F.: Climate change will affect the Asian water towers, Science, 328,
525 1382–1385, https://doi.org/10.1126/science.1183188, 2010.

Jin, X., Jin, H., Luo, D., Sheng, Y., Wu, Q., Wu, J., and Li, Y.: Impacts of permafrost degradation on hydrology and vegetation in the source area of the Yellow River on Northeastern Qinghai-Tibet Plateau, Southwest China, Front. Earth Sci., 10, 845824, https://doi.org/10.3389/feart.2022.845824, 2022.

Kirchner, J. W.: Characterizing nonlinear, nonstationary, and heterogeneous hydrologic behavior using ensemble rainfall–
530 runoff analysis (ERRA): proof of concept, Hydrol. Earth Syst. Sci., 28, 4427–4454, https://doi.org/10.5194/hess-28-4427-2024, 2024.

Kirchner, J. W.: Impulse response functions for nonlinear, nonstationary, and heterogeneous systems, estimated by deconvolution and demixing of noisy time series, Sensors, 22, 3291, https://doi.org/10.3390/s22093291, 2022.

Kornfeld, R. P., Arnold, B. W., Gross, M. A., Dahya, N. T., Klipstein, W. M., Gath, P. F., and Bettadpur, S.: GRACE-FO:
535 the gravity recovery and climate experiment follow-on mission, J. Spacecr. Rockets, 56, 931–951, https://doi.org/10.2514/1.A34326, 2019.

Kuang, X., Liu, J., Scanlon, B. R., Jiao, J. J., Jasechko, S., Lancia, M., and Zheng, C.: The changing nature of groundwater in the global water cycle, Science, 383, eadf0630, https://doi.org/10.1126/science.adf0630, 2024.

Lawrence, D. M. and Slater, A. G.: Incorporating organic soil into a global climate model, Clim. Dyn., 30, 145–160,
540 https://doi.org/10.1007/s00382-007-0278-1, 2008.

Liang, S., Cheng, J., Jia, K., Jiang, B., Liu, Q., Xiao, Z., and Zhou, J.: The global land surface satellite (GLASS) product suite, Bull. Am. Meteorol. Soc., 102, E323–E337, https://doi.org/10.1175/BAMS-D-18-0341.1, 2021.

Li, Z., Feng, Q., Wang, Q. J., Yong, S., Li, J., Li, Y., and Wang, Y.: Quantitative evaluation on the influence from cryosphere meltwater on runoff in an inland river basin of China, Glob. Planet. Change, 143, 189–195,
545 https://doi.org/10.1016/j.gloplacha.2016.06.005, 2016.

Luo, D., Wu, Q., Jin, H., Marchenko, S. S., Lü, L., and Gao, S.: Recent changes in the active layer thickness across the northern hemisphere, Environ. Earth Sci., 75, 1–15, https://doi.org/10.1007/s12665-015-5229-2, 2016.

Luo, D., Jin, H., Bense, V. F., Jin, X., and Li, X.: Hydrothermal processes of near-surface warm permafrost in response to strong precipitation events in the Headwater Area of the Yellow River, Tibetan Plateau, Geoderma, 376, 114531,
550 https://doi.org/10.1016/j.geoderma.2020.114531, 2020.

Ma, Q., Jin, H., Bense, V. F., Luo, D., Marchenko, S. S., Harris, S. A., and Lan, Y.: Impacts of degrading permafrost on streamflow in the source area of Yellow River on the Qinghai-Tibet Plateau, China, Adv. Clim. Change Res., 10, 225–239, https://doi.org/10.1016/j.accre.2020.02.001, 2019.

Martens, B., Miralles, D. G., Lievens, H., Van Der Schalie, R., De Jeu, R. A., Fernández-Prieto, D., et al.: GLEAM v3:
555 Satellite-based land evaporation and root-zone soil moisture, Geosci. Model Dev., 10, 1903–1925, https://doi.org/10.5194/gmd-10-1903-2017, 2017.

Meng, F., Su, F., Yang, D., Tong, K., and Hao, Z.: Impacts of recent climate change on the hydrology in the source region of the Yellow River basin, J. Hydrol. Reg. Stud., 6, 66–81, https://doi.org/10.1016/j.ejrh.2016.03.003, 2016.

560 Meyer, A., Fleischmann, A. S., Collischonn, W., Paiva, R., and Jardim, P.: Empirical assessment of flood wave celerity–discharge relationships at local and reach scales, Hydrol. Sci. J., 63, 2035–2047, https://doi.org/10.1080/02626667.2018.1557336, 2018.

Mu, C., Abbott, B. W., Norris, A. J., Mu, M., Fan, C., Chen, X., et al.: The status and stability of permafrost carbon on the Tibetan Plateau, Earth-Sci. Rev., 211, 103433, https://doi.org/10.1016/j.earscirev.2020.103433, 2020.

Pepin, N., Bradley, R. S., Diaz, H. F., Baraer, M., Caceres, E. B., Forsythe, N., et al.: Elevation-dependent warming in mountain regions of the world, Nat. Clim. Change, 5, 424–430, https://doi.org/10.1038/nclimate2563, 2015.

Qin, D., Yao, T., Ding, Y., and Ren, J. (Eds.): Introduction to cryospheric science, Springer Nature, 2021.

Qin, Y., Yang, D., Gao, B., Wang, T., Chen, J., Chen, Y., et al.: Impacts of climate warming on the frozen ground and eco-hydrology in the Yellow River source region, China, Sci. Total Environ., 605, 830–841, https://doi.org/10.1016/j.scitotenv.2017.06.188, 2017.

570 Qiu, J.: Thawing permafrost reduces river runoff, Nature, 6, https://doi.org/10.1038/nature.2012.9749, 2012.

Rodell, M., and Reager, J. T.: Water cycle science enabled by the GRACE and GRACE-FO satellite missions, Nat. Water, 1, 47–59, https://doi.org/10.1038/s44221-022-00005-0, 2023.

Schuur, E. A., McGuire, A. D., Schädel, C., Grosse, G., Harden, J. W., Hayes, D. J., et al.: Climate change and the permafrost carbon feedback, Nature, 520, 171–179, https://doi.org/10.1038/nature14338, 2015.

575 Sheng, Y., Ma, S., Cao, W., and Wu, J.: Spatiotemporal changes of permafrost in the Headwater Area of the Yellow River under a changing climate, Land Degrad. Dev., 31, 133–152, https://doi.org/10.1002/ldr.3434, 2020.

Sherman, L. K.: The relation of hydrographs of runoff to size and character of drainage‐basins, Eos Trans. Am. Geophys. Union, 13, 332–339, https://doi.org/10.1029/TR013i001p00332, 1932.

Shi, R., Yang, H., and Yang, D.: Spatiotemporal variations in frozen ground and their impacts on hydrological components 580 in the source region of the Yangtze River, J. Hydrol., 590, 125237, https://doi.org/10.1016/j.jhydrol.2020.125237, 2020.

Walvoord, M. A., and Kurylyk, B. L.: Hydrologic impacts of thawing permafrost—A review, Vadose Zone J., 15, vzj2016-01, https://doi.org/10.2136/vzj2016.01.0010, 2016.

Song, L., Wang, L., Luo, D., Chen, D., and Zhou, J.: Assessing hydrothermal changes in the upper Yellow River Basin amidst permafrost degradation, npj Clim. Atmos. Sci., 7, 57, https://doi.org/10.1038/s41612-024-00607-3, 2024.

585 Wang, T., Yang, H., Yang, D., Qin, Y., and Wang, Y.: Quantifying the streamflow response to frozen ground degradation in the source region of the Yellow River within the Budyko framework, J. Hydrol., 558, 301–313, https://doi.org/10.1016/j.jhydrol.2018.01.050, 2018.

Wang, T., Yang, D., Yang, Y., Piao, S., Li, X., Cheng, G., and Fu, B.: Permafrost thawing puts the frozen carbon at risk over the Tibetan Plateau, Sci. Adv., 6, eaaz3513, https://doi.org/10.1126/sciadv.aaz3513, 2020.

590 Wang, T., Yang, D., Yang, Y., Zheng, G., Jin, H., Li, X., et al.: Pervasive permafrost thaw exacerbates future risk of water shortage across the Tibetan Plateau, Earth's Future, 11, e2022EF003463, https://doi.org/10.1029/2022EF003463, 2023a.

Wang, T., Yang, D., Yang, Y., Zheng, G., Jin, H., Li, X., et al.: Unsustainable water supply from thawing permafrost on the Tibetan Plateau in a changing climate, Sci. Bull., 68, 1105–1108, https://doi.org/10.1016/j.scib.2023.04.037, 2023b.

Wang, Y., Yang, H., Gao, B., Wang, T., Qin, Y., and Yang, D.: Frozen ground degradation may reduce future runoff in the
595 headwaters of an inland river on the northeastern Tibetan Plateau, J. Hydrol., 564, 1153–1164, https://doi.org/10.1016/j.jhydrol.2018.07.078, 2018.

Wu, P., Liang, S., Wang, X. S., McKenzie, J. M., and Feng, Y.: Climate change impacts on cold season runoff in the headwaters of the Yellow River considering frozen ground degradation, Water, 12, 602, https://doi.org/10.3390/w12020602, 2020.

600 Yang, J., Wang, T., Yang, D., and Yang, Y.: Insights into runoff changes in the source region of Yellow River under frozen ground degradation, J. Hydrol., 617, 128892, https://doi.org/10.1016/j.jhydrol.2022.128892, 2023.

Yang, K., He, J., Tang, W., Lu, H., Qin, J., Chen, Y., and Li, X.: China meteorological forcing dataset (1979–2018), Natl. Tib. Plateau/Third Pole Environ. Data Cent., https://doi.org/10.11888/AtmosphericPhysics.tpe.249369.file, 2019.

Yang, Y., Wu, Q., Jin, H., Wang, Q., Huang, Y., Luo, D., et al.: Delineating the hydrological processes and hydraulic
605 connectivities under permafrost degradation on Northeastern Qinghai-Tibet Plateau, China, J. Hydrol., 569, 359–372, https://doi.org/10.1016/j.jhydrol.2018.11.068, 2019.

Yao, T., Bolch, T., Chen, D., Gao, J., Immerzeel, W., Piao, S., et al.: The imbalance of the Asian water tower, Nat. Rev. Earth Environ., 3, 618–632, https://doi.org/10.1038/s43017-022-00299-4, 2022.

Yi, S., Wang, X., Qin, Y., Xiang, B., and Ding, Y.: Responses of alpine grassland on Qinghai–Tibetan Plateau to climate
610 warming and permafrost degradation: a modeling perspective, Environ. Res. Lett., 9, 074014, https://doi.org/10.1088/1748-9326/9/7/074014, 2014.

Zhang, T., Barry, R. G., Knowles, K., Heginbottom, J. A., and Brown, J.: Statistics and characteristics of permafrost and ground-ice distribution in the Northern Hemisphere, Polar Geogr., 23, 132–154, https://doi.org/10.1080/10889379909377670, 1999.

615 Zhao, L., Zou, D., Hu, G., Du, E., Pang, Q., Xiao, Y., et al.: Changing climate and the permafrost environment on the Qinghai–Tibet (Xizang) Plateau, Permafrost Periglac. Process., 31, 396–405, https://doi.org/10.1002/ppp.2056, 2020.

Zheng, D., van der Velde, R., Su, Z., Wen, J., Wang, X., and Yang, K.: Impact of soil freeze-thaw mechanism on the runoff dynamics of two Tibetan rivers, J. Hydrol., 563, 382–394, https://doi.org/10.1016/j.jhydrol.2018.06.024, 2018.

Zou, D., Zhao, L., Sheng, Y., Chen, J., Hu, G., Wu, T., et al.: A new map of permafrost distribution on the Tibetan Plateau,
620   Cryosphere, 11, 2527–2542, https://doi.org/10.5194/tc-11-2527-2017, 2017.